Applied Physics A (2022) 128:554
https://doi.org/10.1007/s00339-022-05623-9

Applied Physics A
Materials Science & Processing

Effects of vacancy co-doping on the structure, magnetic and dielectric properties of $LaFeO_3$ perovskite nanoparticles

M. M. Arman[1] · M. A. Ahmed[1]

Received: 23 November 2021 / Accepted: 19 April 2022 / Published online: 4 June 2022

Abstract
Perovskite nanoparticles $La_{1-x}\square_xFe_{1-y}\square_yO_3$, ($y=x=0.0$, 0.01 and 0.02) were prepared using the citrate combustion method. The samples were crystallized in a single phase orthorhombic structure. The energy dispersive spectroscopy (EDS) confirms that the chemical composition is very close to the nominal one. The particle size values indicated that the samples were prepared in nano scale. The selected area electron diffraction (SAED) pattern shows the good crystallinity of the samples. The magnetic hysteresis loops indicate the antiferromagnetic properties of the samples. The molar magnetic susceptibility (χ_M) of $LaFeO_3$ sample was enhanced by vacancy doping. The value of M_s of the sample $La_{0.98}\square_{0.02}Fe_{0.98}\square_{0.02}O_3$ increased by a factor 1.9 than that of sample $LaFeO_3$. The investigated samples have semiconductor-like behavior as clear from the increase in the conductivity with raising the temperature and the values of activation energies. The main conduction mechanisms in the investigated samples are the small polaron tunneling (SP) and the correlated barrier hopping (CBH).

Keywords Perovskites · $LaFeO_3$ · Nanoparticles · Vacancy substitution

1 Introduction

The perovskite materials have a general formula of ABO_3, where A is a rare earth element and is coordinated by 12 oxygen anions. While B cation is a 3d transition metal and coordinated to six oxygen anions. Metals with different oxidation states can be replaced by the metal ions at the A and B sites due to the great stability of the ABO_3 materials [1]. Thus, novel materials can be designed with various properties for different applications.

Lanthanum orthoferrite ($LaFeO_3$) has a perovskite structure with space group Pbnm and has attracted great interest due to its unique physical and chemical properties. $LaFeO_3$ has G-type antiferromagnetic (AFM) behavior with a Nèel temperature (T_N) ~ 730 K [2]. The ordering of ferroelectric or antiferroelectric dipole moments determines the electrical properties of $LaFeO_3$. The $<FeO_6>$ octahedron in $LaFeO_3$ drives the coexisting magnetic and electrical configurations. The perovskite $LaFeO_3$ was synthesized using different methods such as electrochemical [3], solid-state [4], and sol–gel combustion [5, 6] techniques. $LaFeO_3$ was prepared in nano scale easily using the citrate nitrate combustion method [7].

The perovskite structure ABO_3 contains an equal amount of A and B site cations (i.e., the A/B cation ratio = 1). When the A/B cation ratio is deviated significantly from unit, the perovskite lattice structure can still be stable. Introduction of the vacancy on both A and B cation sites tilts the $<BO_6>$ octahedron. The octahedral tilting lowers the coordination number of the A cation from 12 to 8 [8], reducing the tension in A–O bonds and increasing lattice energy. The presence of an octahedral tilting distortion affects not only the crystal structure, but also has a profound influence on the physical properties such as electrical conductivity, magnetic superexchange interactions and other electrical properties [9]. The nonstoichiometric A-site cation perovskite ABO_3 were developed as cathodes for solid-oxide fuel cells (SOFCs) and improve the oxygen reduction reaction (ORR) activity at high temperatures [10, 11].

Spinicci et al. [12] were prepared $La_{(1-\varepsilon)}FeO_{(3-1.5\varepsilon)}$ with $\varepsilon=0.0$, 0.1, 0.2, 0.3 using thermal low-temperature decomposition, a method which ensures a high surface area. $La_{(1-\varepsilon)}FeO_{(3-1.5\varepsilon)}$ have been used in catalytic methane combustion in the range 300–450 °C. Scafetta et al. [13] have studied the effect of La and Fe deficiency on the *c*-axis

✉ M. M. Arman
mmarmsci@gmail.com

[1] Materials Science Lab (1), Physics Department, Faculty of Science, Cairo University, Giza, Egypt

lattice parameter and optical absorption in $La_{1-x}Fe_{1-y}O_{3-\delta}$ films. Fe vacancies expanded out-of-plane lattice parameters while La deficiency leads to an increase in absorption throughout the spectral range probed. Zhu et al. [14] prepared the A-site cation deficient perovskites ($La_{0.95}FeO_{3-\delta}$) by a simple and cost-effective process. $La_{0.95}FeO_{3-\delta}$ samples have highly-efficient bifunctional electrocatalysts for ORR and oxygen evolution reaction (OER) in alkaline solutions.

Arman et al. [15] were investigated the effect of cation deficiency on $NdFeO_3$. The self-doped vacancies on A and B sites of $NdFeO_3$ increased the saturation magnetization (M_s) of the sample $Nd_{0.97}\square_{0.03}Fe_{0.97}\square_{0.03}O_3$ by 1.5 times more than the parent sample $NdFeO_3$. The antiferromagnetic properties of $NdFeO_3$ perovskite were originated from magnetic interactions such as Nd–Nd, Nd–Fe, and Fe–Fe. While $LaFeO_3$ has Fe–Fe magnetic interaction only. The difference in ionic radii of La^{3+} ion (1.216 Å) and that of Nd^{3+} ion (1.163 Å) affects the tolerance factor and tilting of $<BO_6>$ octahedron.

In this present work, we studied the effect of vacancy co-doping on the physical properties such as the magnetic and dielectric properties of $LaFeO_3$ nanoparticles. The substitution of the vacancy on both A and B cation sites simultaneously is influenced by the structure, morphology and all physicochemical properties of the samples. The introduced A and B- site cation vacancies in $LaFeO_3$ enhanced Fe–Fe magnetic interaction and improved the hybridization between the La 3d and O 2p states. Furthermore, the presence of La and Fe defects increases the specific surface area. The vacancy doped samples are more applicable in many applications, such as the heavy metal removal from wastewater, cathode catalysts for lithium-oxygen (Li-O_2) batteries [16–18].

2 Experimental techniques

The perovskite samples $La_{1-x}\square_xFe_{1-y}\square_yO_3$, ($0.0 \le y, x \le 0.02$, step 0.01) were prepared by citrate nitrate combustion method [14, 16]. The precursor metal nitrates (purity 99.9%, Sigma–Aldrich) were mixed in stoichiometric ratios with an equivalent molar ratio of citric acid in aqueous media to enhance the homogeneous mixing. To produce La and Fe vacancies, the $La(NO_3)_3{\bullet}6H_2O$ and $Fe(NO_3)_3{\bullet}9H_2O$ are stoichiometrically decreased by 1% and 2% to generate non-stoichiometric La and Fe defects. The $LaFeO_3$ perovskite has a stable structure upto 30% nonstoichiometric La and Fe defects [12, 16]. To ensure complete complexation, the pH value was adjusted to 7 using the ammonia solution as a fuel. The (citric acid/nitrate) ratio is kept constant for all samples and is equal to 1. The samples were heated on a hot plate to obtain the final product that gives a fluffy powder with a single-phase orthorhombic structure. Thermal dehydration resulted in a highly viscous liquid. The citrate nitrate combustion method is simple, low cost, and quick.

X-ray powder diffraction (XRD) was carried out to study the crystal structure of the samples using a Proker D8 advanced X-ray diffractometer with Cu-Kα radiation ($\lambda = 1.5418$ Å). The crystalline phases of the samples were identified using the International Centre for Diffraction Data (ICDD) card number 74–2203.

The samples were characterized by scanning electron microscopy (SEM) and energy dispersive spectroscopy (EDS) to study the morphology of the samples using OXFORD INCA PentaFETX3-England. The shape and size of the particles were studied using a high-resolution transmission electron microscope (HRTEM) model (JEOl-2100). The magnetic properties of the samples were studied by two techniques: the first is the H-M hysteresis loop using a vibrating sample magnetometer (VSM; 9600–1 LDJ, USA) with a maximum applied field of 20 kOe at room temperature. While the second technique is measurements of dc magnetic susceptibility (χ_M) using Faraday's method [19] at different magnetic field intensities as a function of absolute temperature.

The powdered samples were pressed to obtain pellets using a press of value 8×10^5 N/m^2 [7]. The two surfaces of each pellet were checked for good conduction by coating the surfaces with silver paste. The electrical properties were measured on pellets of samples using the LCR meter (Hioki model 3532 Japan). The dielectric constant (ε′) and ac conductivity of the samples were measured as a function of temperature in the frequency range 100 Hz to 5 MHz. The data was triplet and taken the average value.

3 Results and discussion

Figure 1 illustrates the XRD patterns of the samples that have the formula of $La_{1-x}\square_xFe_{1-y}\square_yO_3$, ($0.0 \le y, x \le 0.02$, step 0.01). The prepared samples were crystallized in a single phase orthorhombic structure with space group Pbnm. The data was indexed with ICDD card number 74–2203. The main peak (100%) of $LaFeO_3$ is observed for (200) plane at $2\theta = 34.5°$. The lattice parameters (a, b and c) were calculated based on orthorhombic unit cell from Eq. (1) and listed in Table 1. The crystallite size (L) was determined using Scherrer's equation which is given by Eq. (2). [20]

$$\frac{1}{d^2} = \frac{h^2}{a^2} + \frac{k^2}{b^2} + \frac{l^2}{c^2} \tag{1}$$

$$L = \frac{0.9\lambda}{\beta \cos\theta}, \tag{2}$$

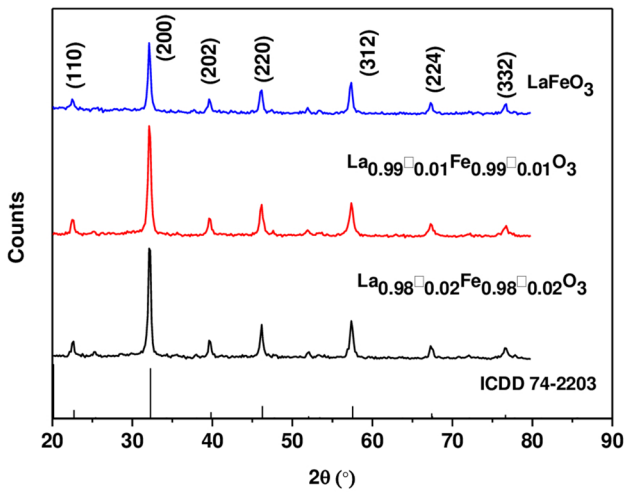

Fig. 1 XRD of the samples $La_{1-x}\square_xFe_{1-y}\square_yO_3$ as compared with ICDD card number 74–2203. The main peak (100%) is observed for (200) plane at $2\theta = 34.5°$

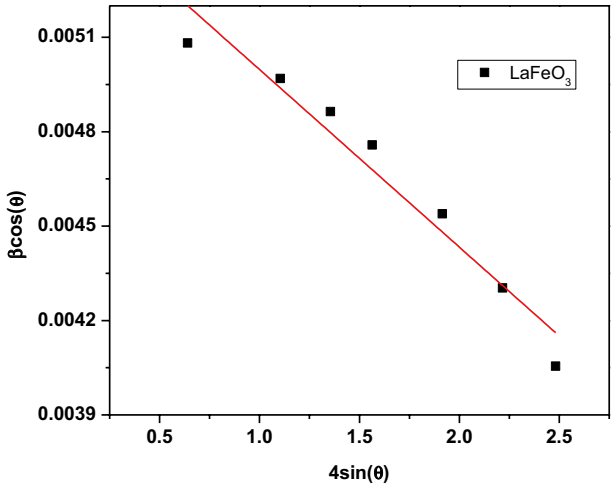

Fig. 2 The Williamson–Hall plot for $LaFeO_3$ sample. The crystallite size (L_{WH}) was calculated from the intercept of the fitting line with y-axis

where L is the average crystallite size, θ is the Bragg angle, λ is the wave length of the X-ray radiation ($\lambda = 1.5406$ Å), and β is the full width at half maximum intensity of the powder pattern peak. The values of L were listed in Table 1 and indicated that the samples are prepared in nano scale.

The crystallite size (L_{WH}) of the samples and the average lattice strain (ε) were calculated using the well-known Williamson–Hall equations [21]:

$$\beta \cos\theta = 4\varepsilon \sin\theta + \frac{K\lambda}{L_{WH}}, \tag{3}$$

where K is the dimensionless shape factor ($K = 0.9$) and θ is the Bragg angle. Figure 2 illustrates the relation between $\beta\cos\theta$ and $4\sin\theta$. The value of ε was determined from the slope of the plot in Fig. 2 and reported in Table 1. The crystallite size (L_{WH}) was calculated from the intercept of the fitting line with y-axis and its values confirm that the samples were crystallized in nano scale. The W–H plot shows the negative value of the strain and indicates the compressive nature of it which leads to lattice shrinkage [18].

The unit cell volume and the theoretical density were calculated using the following equations, respectively.

$$V = abc \tag{4}$$

$$D_x = \frac{ZM}{N_A V}, \tag{5}$$

where Z ($Z = 4$) is the number of molecules per unit cell, N_A is the Avogadro's number, M is the molecular weight, and V is the unit cell volume. The values of D_x of the vacancy-doped samples are less than that of $LaFeO_3$ owing to the decrease of La^{3+} and Fe^{3+} content with investigated samples. The values of experimental density were calculated using the relation $D_{exp} = \frac{m}{V}$ and reported in Table 1. The values of D_{exp} are smaller than the theoretical density owing to oxygen deficiency.

The tolerance factor was calculated using the following equation [22]:

$$t = \frac{r_A + r_O}{\sqrt{2}(r_B + r_O)}, \tag{6}$$

Table 1 Values of the lattice parameters, the unit cell volume (V), the theoretical density (D_x), the crystallite size from XRD (L), Williamson–Hall crystallite size (L_{WH}), micro strain (□), the particle size (L) and the tolerance factor for the investigated samples

Samples	a (Å) (0.0001)	b (Å) (0.0001)	c (Å) (0.0001)	V (Å^3) (0.1)	D_x (g/cm^3) (0.0002)	D_{exp} (g/cm^3) (0.0002)	L (XRD) (nm) (0.5)	L_{WH} (nm)	L (HREM) (nm) (0.5)	ε 10^{-4}	t (0.0002)
$x=y=0.00$	5.5372	5.6066	7.8471	243.615	6.6182	2.8660	34	25	29	5.645	0.9550
$x=y=0.01$	5.5525	5.5575	7.8116	240.804	6.0334	5.3969	26	22	38	6.265	0.9531
$x=y=0.02$	5.5615	5.5457	7.8505	242.132	5.9578	2.4812	28	24	62	5.884	0.9514

Table 2 The composition of weight percentage (wt%) for the samples (a) $LaFeO_3$, (b) $La_{0.99}\square_{0.01}Fe_{0.99}\square_{0.01}O_3$ and (c) $La_{0.98}\square_{0.02}Fe_{0.98}\square_{0.02}O_3$ as obtained from EDS

Elements	(a) $LaFeO_3$		(b) $La_{0.99}\square_{0.01}Fe_{0.99}\square_{0.01}O_3$		(c) $La_{0.98}\square_{0.02}Fe_{0.98}\square_{0.02}O_3$	
	Weight percentage (wt%)		Weight percentage (wt%)		Weight percentage (wt%)	
	From EDX	Theoretically	From EDX	Theoretically	From EDX	Theoretically
O K	23.39	19.77	21.82	19.93	19.28	20.10
Fe K	20.95	23.01	23.23	22.96	23.36	22.91
La L	55.66	57.22	54.94	57.11	57.36	56.99

where r_A, r_B and r_O are the ionic radii of the A, B and oxygen ions respectively. The values of tolerance factors were listed in Table 1. The tolerance factor (t) is less than 1 which indicates that tilting of the $<BO_6>$ octahedra occurs for all the samples. The tolerance factor indicates the orthorhombic structure of the samples $La_{1-x}\square_xFe_{1-y}\square_yO_3$ and these results agree with the data obtained from XRD analysis. The values of the tolerance factor decrease with increasing the vacancy content (x and y) at the expense of La^{3+} and Fe^{3+} ions, which means that the distortion of the perovskite unit cell increases. This means that the Fe–O–Fe angle decreases with increasing the vacancy content (x and y). On the other hand, the tilting angle decreases. Besides, the values of t ($0.9550 < t < 0.9514$), indicated that the structure distorts.

To confirm the chemical composition of the samples, the energy dispersive spectroscopy EDS analysis was performed. Table 2 illustrates the EDS data of the investigated samples. The figure shows that the prepared samples are nearly equal to the starting chemical composition without any noticeable impurities. The weight percentage (wt%) of elements (La, Fe, and O) are calculated theoretically from the chemical formula $La_{1-x}\square_xFe_{1-y}\square_yO_3$, ($0.0 \le y$, $x \le 0.02$, step 0.01) and that obtained from EDS elemental analysis are shown in Table 2. The results confirm that the chemical composition is very close to the nominal one. The small variation between the values of weight percentage (wt%) (La, Fe, and O) due to oxygen deficiency and converting some Fe^{3+} to Fe^{2+}.

Figure 3 shows HRTEM images of the samples $La_{1-x}\square_xFe_{1-y}\square_yO_3$. The images illustrate the orthorhombic structure of nanocrystalline samples. The values of particle size were listed in Table 1 and indicated that the samples were prepared in nano scale. The values of particle size agree with those obtained from XRD. The particles are agglomerated as shown in Fig. 3 owing to the magnetic properties of the samples. Different brightness from one crystallite to another appears as a result of different orientations of the crystal structure. The insets in Fig. 3 show the d-spacing of the investigated samples with values 0.26, 2.5 and 0.49 nm of the samples $La_{1-x}\square_xFe_{1-y}\square_yO_3$, ($0.0 \le x$ and $y \le 0.02$, step 0.01), respectively. The selected area electron diffraction (SAED) pattern of the investigated samples is illustrated in the insets in Fig. 3. The patterns show the good crystallinity of the samples.

Figure 4 shows the relation between the molar magnetic susceptibility (χ_M) and the absolute temperature for $LaFeO_3$ nanoparticles. The sample has antiferromagnetic behavior where the values of χ_M decreased rapidly with temperature until the Néel temperature then decreased slowly with temperature. The magnetic interactions originated from the superexchange interaction between the Fe^{3+} ions, while there is no magnetic interaction between La^{3+} ion and Fe^{3+} ion because La^{3+} ion is not magnetic. By increasing the vacancies in the sample, the tilting of $<FeO_6>$ octahedron increases, leading to a weak ferromagnetic ordering along with other crystal directions [23].

The comparative study between the vacancy doped samples in the molar magnetic susceptibility at the magnetic field intensity 1100 Oe is illustrated in Fig. 5. χ_M increases with increasing the vacancies on the A and B sites. The reasons for the increase of χ_M are:

(1) Some of the Fe^{3+} ions convert to Fe^{4+} ions, which create the three magnetic interactions (antiferromagnetic between Fe^{3+}–Fe^{3+} and Fe^{4+}–Fe^{4+}, ferromagnetic between Fe^{3+}–Fe^{4+}).
(2) The tilting of $<FeO_6>$ octahedron affects the bond length and strength between Fe–O ions.

The Curie–Weiss law is satisfied in the investigated samples. The straight lines in the paramagnetic region of $LaFeO_3$ sample at 1100 Oe in the temperature range of 850–910 K are shown in Fig. 6.[15] The values of the Curie constant (C), Curie–Weiss constant (θ), and the effective magnetic moment (μ_{eff}) are calculated from the reciprocal of magnetic susceptibility with absolute temperature and reported in Table 3 using the following equations:

$$C = \frac{1}{\text{slope}} \tag{7}$$

$$\mu_{eff} = 2.83\sqrt{C}. \tag{8}$$

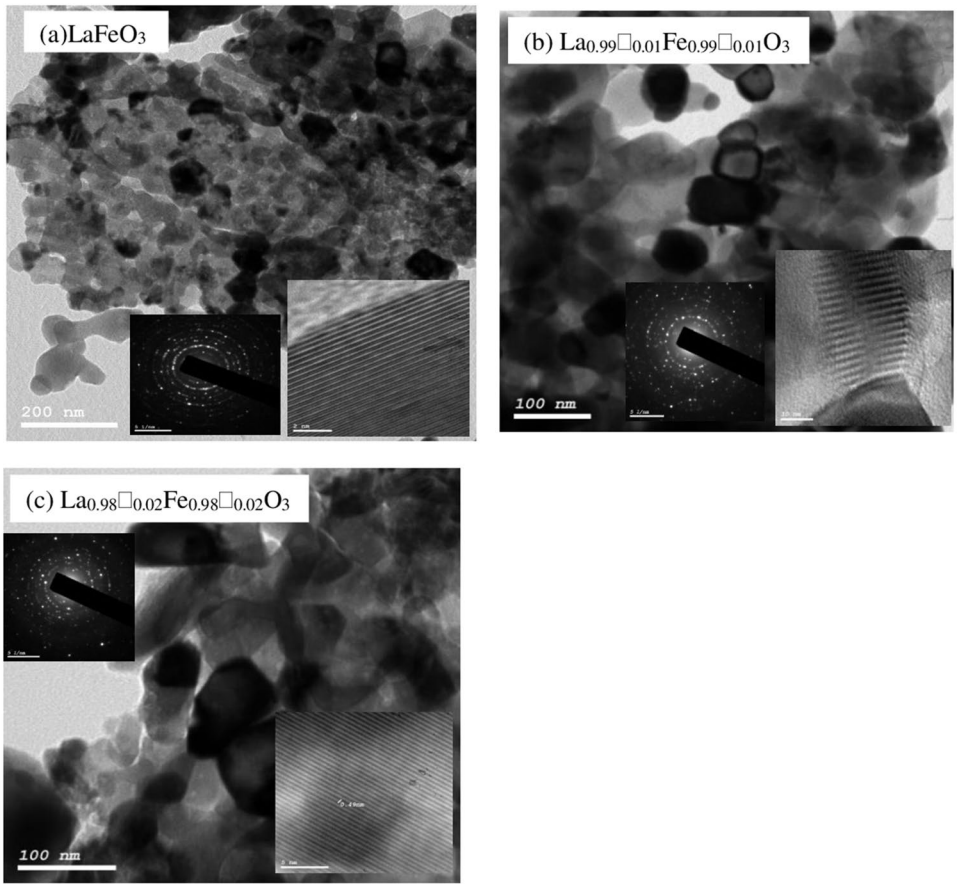

Fig. 3 HRTEM images for the samples **a** $LaFeO_3$, **b** $La_{0.99}\square_{0.01}Fe_{0.99}\square_{0.01}O_3$ and **c** $La_{0.98}\square_{0.02}Fe_{0.98}\square_{0.02}O_3$ with average particle size 29 nm, 38 nm and 62 nm respectively. The insets illustrate d-spacing and SAED for the samples

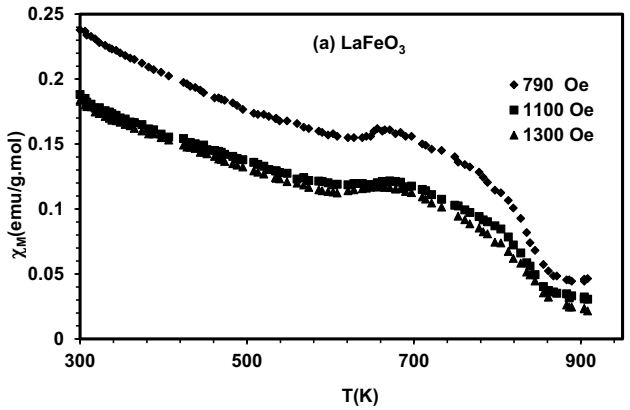

Fig. 4 The relation between the molar magnetic susceptibility and the absolute temperature for the sample $LaFeO_3$, at different magnetic field intensities. The sample has antiferromagnetic behavior

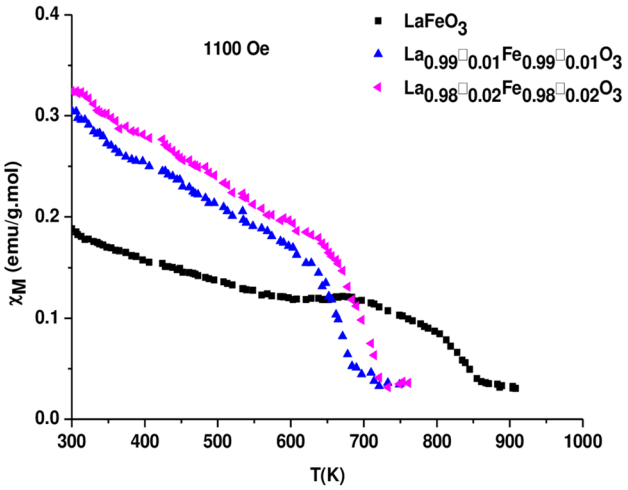

Fig. 5 A comparative study of the molar magnetic susceptibility for the samples $La_{1-x}\square_xFe_{1-y}\square_yO_3$ at magnetic field intensity 1100 Oe. The vacancies on the A and B sites enhanced the magnetization of the samples

The presence of a ferromagnetic component in the samples was illustrated by the positive values of θ. The Néel temperature of the samples was determined from the plots of (dM/dT) vs T where M is the magnetization.

Figure 7 illustrates the hysteresis loops of the samples $La_{1-x}\square_xFe_{1-y}\square_yO_3$, ($0.0 \le x$, $y \le 0.02$, step 0.01) at room temperature. The S-shape of the hysteresis loops indicates the presence of a weak ferromagnetic component in addition to the main antiferromagnetic order in the samples. The

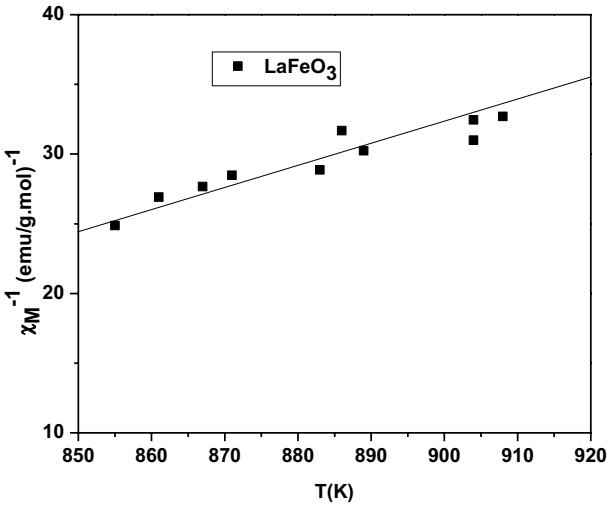

Fig. 6 Dependence of the reciprocal molar magnetic susceptibility in paramagnetic region for $LaFeO_3$ at magnetic field intensity 1100 Oe

Table 3 Values of the Curie constant (C), the Curie–Weiss constant (θ), the effective magnetic moment (μ_{eff}) and the Neel temperatures of the samples $La_{1-x}\square_xFe_{1-y}\square_yO_3$ at magnetic field intensity of 1100 Oe

Samples	C (emu/g. mol) K (0.005)	θ (K) (1)	μ_{eff} (B.M.) (0.005)	T_N (K) (1)
$LaFeO_3$ (parent)	5.42	655	6.58	845
$La_{0.99}\square_{0.01}Fe_{0.99}\square_{0.01}O_3$	2.92	800	4.83	833
$La_{0.98}\square_{0.02}Fe_{0.98}\square_{0.02}O_3$	5.88	770	6.86	824

magnetic parameters such as saturation magnetization (M_s) and remnant magnetization (M_r) are listed in Table 4. The value of saturation magnetization M_s of $LaFeO_3$ agrees with the data published by Gabala et al. [24]. The magnetization of the $LaFeO_3$ sample was enhanced by vacancy doping. The value of M_s of the sample $La_{0.98}\square_{0.02}Fe_{0.98}\square_{0.02}O_3$ increased by the factor 1.9 compared with the sample $LaFeO_3$. The improvement of magnetic parameters for vacancy doped samples can be ascribed to several reasons as follows: (i) The tilting of $<FeO_6>$ induces a variation in the Fe–O–Fe bond angle and distance; (ii) The existence of Fe^{3+} (HS) (t_{2g}^3 e_g^2) and Fe^{4+} ions in high spin state (HS) Fe^{4+} (t_{2g}^3 e_g^1) [7].

The inset in Fig. 7 illustrates the hysteresis loop of the parent sample ($LaFeO_3$) has a clear shift from the origin due to the exchange bias effect. The exchange bias field (H_{EB}) was calculated using Eq. (9):

$$H_{EB} = -\left(H_{Left} + H_{right}\right)/2, \tag{9}$$

where H_{Left} and H_{right} are the intercept of the magnetization on the −ve and +ve on the H-axis. The values of exchange bias were reported in Table 4. The exchange bias is present due to the exchange coupling between the ferromagnetic-like shell and the antiferromagnetic core in the nanoparticle [25].

Figure 8 illustrates the dependence of the dielectric constant on the absolute temperature of the sample $La_{0.99}\square_{0.01}Fe_{0.99}\square_{0.01}O_3$. The trend of ε' of the sample is the general trend of dielectric materials where ε' increases with increasing the temperature and decreases with increasing the frequency.

Figure 9 shows the dependence of lnσ on the reciprocal of absolute temperature (1000/T) as a function of frequencies for the sample $La_{0.99}\square_{0.01}Fe_{0.99}\square_{0.01}O_3$. The plot data obeys the well-known Arrhenius equation [26]:

$$\sigma = \sigma_o \exp\left(-E/kT\right), \tag{10}$$

where E is the activation energy, k is the Boltzmann's constant and T is the absolute temperature. The presence of two different straight lines indicates the presence of two conduction mechanisms in the investigated samples. The activation energies were calculated and reported in Table 5 using the Arrhenius equation at frequency 5 MHz. The activation energy in the high temperature region (E_{II}) is greater than that of low temperature (E_I). The presence of two activation energies is due to the presence of two conduction mechanisms, which are the small polaron (SP) tunneling and the correlated barrier hopping (CBH) as shown in the next section.

The samples have semiconducting like behavior as clear from the increase in the conductivity with an increase of temperature. The values of activation energies confirm the semiconducting trend of the samples. The cation deficient in perovskite $LaFeO_3$ played an important role in the enhancement of the conductivity. Introducing of vacancies in $LaFeO_3$ leads to formation oxygen deficiency and converting

Table 4 Values of the saturation magnetization (M_s), the coercive field (H_c), the remanence magnetization (M_r) and the exchange bias field (H_{EB}) for the samples

Samples	Positive M_s (0.01) (emu/g)	Negative M_s (emu/g) (0.01)	Positive H_c (Oe) (1)	Negative H_c (Oe) (1)	Positive M_r (emu/g) (0.01)	Negative M_r (emu/g) (0.01)	H_{EB} (0.01)
$x=y=0.00$ (parent)	1.52	− 1.60	295.78	− 70.79	0.14	− 0.23	− 112.49
$x=y=0.01$	2.54	− 2.54	143.34	− 145.61	0.33	− 0.33	1.13
$x=y=0.02$	2.84	− 2.83	159.28	− 162.95	0.43	− 0.42	1.84

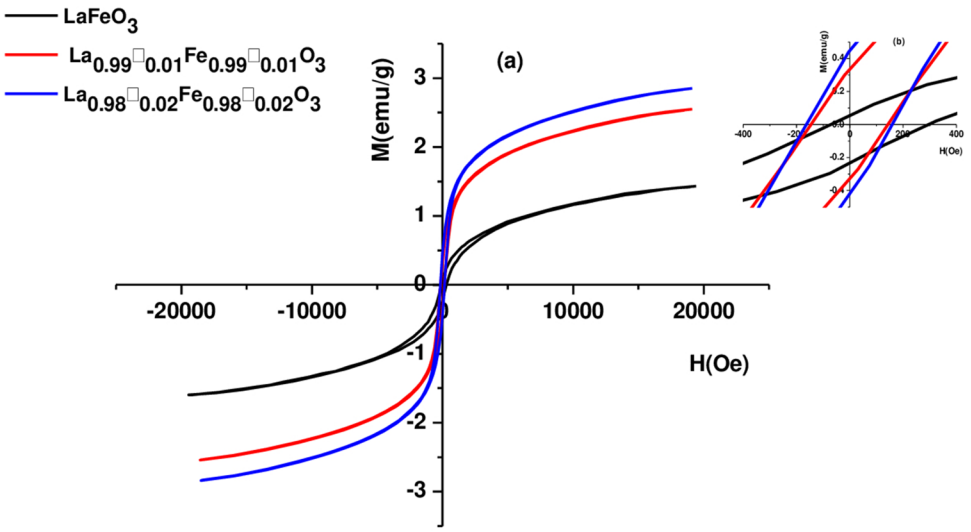

Fig. 7 VSM of the samples $La_{1-x}\square_xFe_{1-y}\square_yO_3$ at room temperature. The inset shows the shift of hysteresis loop from the origin for the parent sample ($LaFeO_3$)

some of Fe^{3+} ions to Fe^{4+} ions ($t_{2g}^3\ e_g^1$ configuration). This will bring a localized electronic structure and lead to an inherent semiconductor nature [16].

Figure 10 illustrates the dependence of lnσ on lnω at different temperatures. The relation between lnσ and lnω obeys the universal power law. [27]

$$\sigma_{ac}(\omega) = A\omega^s, \tag{11}$$

where σ_{ac} is the ac conductivity, $\omega = 2\pi f$ is the angular frequency, A is a temperature dependent constant and S is the frequency dependent exponent. Figure 11 shows the relation between the frequency exponent factor (S) and T. In the 1st temperature region (300–450 K), the increase of S with T which indicates the small polaron (SP) tunneling in this region. This originated from converting some of the Fe^{3+} to Fe^{4+} ions, also, the electron conduction in perovskite-type ferrites takes place through Fe^{4+}–O–Fe^{3+} [28]. While in the 2nd temperature region (450–800 K), S decreases with T which illustrates that the correlated barrier hopping (CBH) is the main mechanism. The electrons accept enough energy to hop between the O 2p and the Fe 3d orbitals. The hopping of electrons is affected by the Fe–O distance and the Fe–O–Fe angle. The values of the activation energy (E_Π) increased in the off-stoichiometric samples owing to the presence of oxygen vacancies [13].

Table 5 Values of the activation energy E_{II} (at high temperature region) and E_I (at low temperature) of the samples $La_{1-x}\square_xFe_{1-y}\square_yO_3$ at frequency 5 MHz

Samples	E_I (eV) (0.01)	E_{II} (eV) (0.01)
$LaFeO_3$	0.17	1.05
$La_{0.99}\square_{0.01}Fe_{0.99}\square_{0.01}O_3$	0.16	1.57
$La_{0.98}\square_{0.02}Fe_{0.98}\square_{0.02}O_3$	0.16	1.70

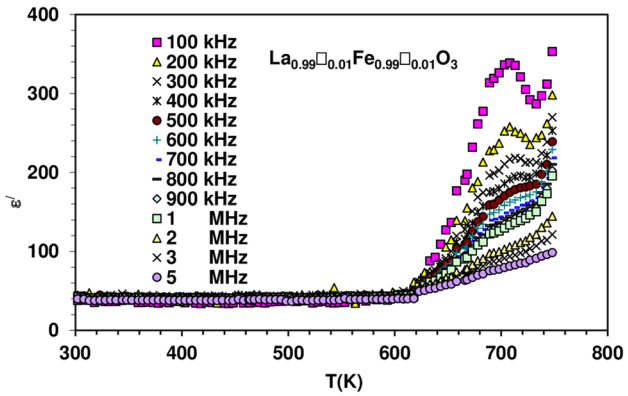

Fig. 8 Dependence of dielectric constant (ε') on absolute temperature T (K) of the sample $La_{0.99}\square_{0.01}Fe_{0.99}\square_{0.01}O_3$ as a function of frequencies. ε' values increases with increasing the temperature and decreases with increasing the frequency

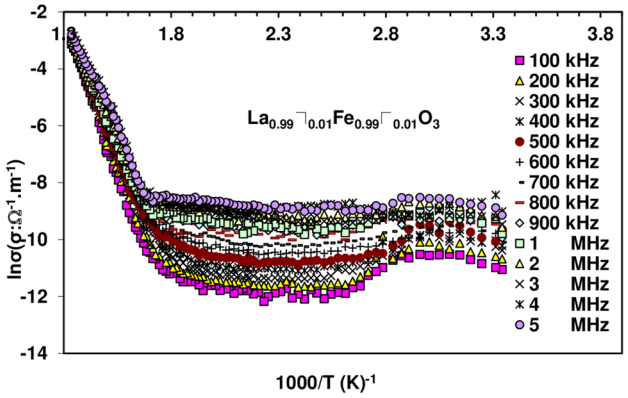

Fig. 9 The dependence of lnσ on the reciprocal of the absolute temperature as a function of frequencies of the sample $La_{0.99}\square_{0.01}Fe_{0.99}\square_{0.01}O_3$

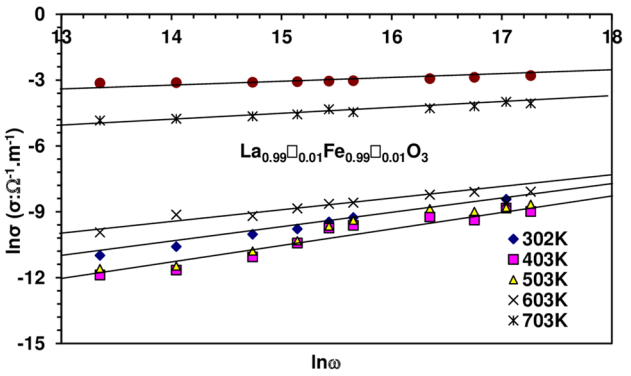

Fig. 10 The relation between the lnσ as a function of lnω at different temperatures of the sample $La_{0.99}\square_{0.01}Fe_{0.99}\square_{0.01}O_3$. The data obeys the universal power law

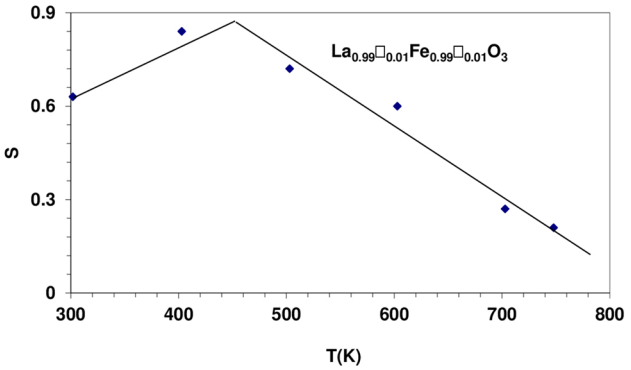

Fig. 11 Relation between the frequency exponent factor (S) and absolute temperature (T) for the sample $La_{0.99}\square_{0.01}Fe_{0.99}\square_{0.01}O_3$. The main conduction mechanisms are the small polaron tunneling (SP) and the correlated barrier hopping (CBH)

4 Conclusion

Orthoferrite of formula $La_{1-x}\square_xFe_{1-y}\square_yO_3$, $(0.0 \le y, x \le 0.02$, step 0.01) were well synthesized using the citrate combustion technique. XRD revealed that the investigated samples crystallized in a single phase orthorhombic structure with space group Pbnm. The particle size of $LaFeO_3$ increased gradually with increasing the vacancy content. The magnetic hysteresis loops indicate the antiferromagnetic properties of the samples. χ_M of $La_{0.98}\square_{0.02}Fe_{0.98}\square_{0.02}O_3$ increased by a factor 1.7 times more than of $LaFeO_3$ sample. The investigated samples have semiconducting-like behavior as clear from the increase in the conductivity with the temperature and the values of activation energies. The small polaron tunneling (SP) and the correlated barrier hopping (CBH) are the main conduction mechanisms in the samples.

Acknowledgements The authors acknowledge deeply S.I. El-Dek (Faculty of Postgraduate Studies for Advanced Sciences (PSAS), Beni-Suef University, Beni-Suef, Egypt) for her nice cooperation and her kind support.

Funding Open access funding provided by The Science, Technology & Innovation Funding Authority (STDF) in cooperation with The Egyptian Knowledge Bank (EKB).

Declarations

Conflict of interest All authors declare that they have no conflict of interest.

References

1. U.F. Vogt, P. Holtappels, J. Sfeir, J. Richter, S. Duval, D. Wiedenmann, A. Züttel, Fuel Cells **9**, 899 (2009)
2. M.A. Ahmed, M.S. Selim, M.M. Arman, Mater. Chem. Phys. **129**, 705 (2011)
3. X.-D. Zhou, J.B. Yang, E.-C. Thomsen, Q. Cai, B.J. Scarfino, Z. Nie, G.W. Coffey, W.J. James, W.B. Yelon, H.U. Anderson, J. Electrochem. Soc. **153**, J133 (2006)
4. M. Idrees, M. Nadeem, M. Mehmood, M. Atif, K.H. Chae, M.M. Hassan, J. Phys. D. Appl. Phys. **44**, 105401 (2011)
5. A.A. Saad, W. Khan, P. Dhiman, A.H. Naqvi, M. Singh, Electron. Mater. Lett. **9**, 77 (2013)
6. M.M. Arman, S.I. El-Dek, J. Phys. Chem. Solids **152**, 109980 (2021)
7. M.M. Arman, M.A. Ahmed, S.I. El-Dek, J. Supercond. Nov. Magn. **31**, 1867 (2018)
8. I.D. Brown, Acta Crystallogr. Sect. B Struct. Sci. **48**, 553 (1992)
9. H.Y. Hwang, T.T.M. Palstra, S.-W. Cheong, B. Batlogg, Phys. Rev. B **52**, 15046 (1995)
10. Y.L. Zhu, Z.-G. Chen, W. Zhou, S.S. Jiang, J. Zou, Z.P. Shao, Chemsuschem **6**, 2249 (2013)
11. F.F. Dong, M. Ni, Y.B. Chen, D.J. Chen, M.O. Tadé, Z.P. Shao, J. Mater. Chem. A **2**, 20520 (2014)
12. R. Spinicci, A. Tofanari, A. Delmastro, D. Mazzab, S. Ronchetti, Mater. Chem. Phys. **76**, 20 (2002)
13. M.D. Scafetta, S.J. May, Phys. Chem. Chem. Phys. **19**, 10371 (2017)
14. Y. Zhu, W. Zhou, J. Yu, Y. Chen, M. Liu, Z. Shao, Chem. Mater. **28**, 1691 (2016)
15. M.M. Arman, M.A. Ahmed, S.I. El-Dek, Appl. Phys. A **126**, 27 (2020)
16. D. Du, R. Zheng, M. He, C. Zhao, B. Zhou, R. Li, H. Xu, X. Wen, T. Zeng, C. Shu, Energy Storage Mater. **43**, 293 (2021)
17. M. M. Arman, J. Supercond. Novel Magn., 1–9 (2022)
18. E. E. Ateia, M. A. Ateia, M. M. Arman, J. Mater. Sci.: Mater. Electron. 1–12 (2021)

19. H. Shen, J. Xu, A. Wu, J. Zhao, M. Shi, Mater. Sci. Eng. B **157**, 77 (2009)
20. M.M. Arman, N.G. Imam, R.L. Portales, S.I. El-Dek, J. Magn. Magn. Mater. **513**, 167097 (2020)
21. V.D. Mote, Y. Purushotham, B.N. Dole, J. Theor. Appl. Phys. **6**, 1 (2012)
22. E.E. Ateia, M.M. Arman, M. Morsy, Appl. Phys. A **125**, 1 (2019)
23. H. Shen, G. Cheng, A. Wu, J. Xu, J. Zhao, Phys. Status Solidi A **206**, 1420–1424 (2009)
24. M.A. Gabal, F. Al-Solami, Y.M. Al Angari, A.A. Ali, A.A. Al-Juaid, K.W. Huang, M. Alsabban, Ceram. Int. **45**, 160 (2019)
25. K. Mukhopadhyay, A.S. Mahapatra, P.K. Chakrabarti, J. Magn. Magn. Mater. **329**, 133–141 (2013)
26. R. Ramadan, S.I. El-Dek, M.M. Arman, Appl. Phys. A **126**, 900 (2020)
27. S.R. Elliott, Adv. Phys. **36**, 135–218 (1987)
28. Y. Ren, R. Küngas, R.J. Gorte, C. Deng, Solid State Ion. **212**, 47–54 (2012)